

Volume 62 Number 10 October 2024

ISSN 0888-323X

Vehicle  
System  
Dynamics

International Journal  
of Vehicle Mechanics  
and Mobility

Official Organ of the

Editor

International Association  
for Vehicle Systems  
Dynamics

Mehdi Ahmadi  
Shinichi Horie  
Klaus Jüttke  
Masoud Pachai

Taylor & Francis  
Taylor & Francis Group

# Vehicle System Dynamics

International Journal of Vehicle Mechanics and Mobility

ISSN: (Print) (Online) Journal homepage: [www.tandfonline.com/journals/nvsd20](http://www.tandfonline.com/journals/nvsd20)

Taylor & Francis  
Taylor & Francis Group

## Beyond the stable handling limits: nonlinear model predictive control for highly transient autonomous drifting

Jonathan Y. M. Goh, Michael Thompson, James Dallas & Avinash Balachandran

**To cite this article:** Jonathan Y. M. Goh, Michael Thompson, James Dallas & Avinash Balachandran (2024) Beyond the stable handling limits: nonlinear model predictive control for highly transient autonomous drifting, *Vehicle System Dynamics*, 62:10, 2590-2613, DOI: [10.1080/00423114.2023.2297799](https://doi.org/10.1080/00423114.2023.2297799)

**To link to this article:** <https://doi.org/10.1080/00423114.2023.2297799>



© 2024 Toyota Research Institute. Published by Informa UK Limited, trading as Taylor & Francis Group



[View supplementary material](#)



Published online: 21 Feb 2024.



[Submit your article to this journal](#)



Article views: 2474



[View related articles](#)



[View Crossmark data](#)



Citing articles: 11 [View citing articles](#)



# Beyond the stable handling limits: nonlinear model predictive control for highly transient autonomous drifting

Jonathan Y. M. Goh, Michael Thompson, James Dallas and Avinash Balachandran

Extreme Vehicle Dynamics Control, Toyota Research Institute, Los Altos, CA, USA

## ABSTRACT

Autonomous vehicles that can reliably operate outside the stable handling limits would have access to a wider range of maneuvers in emergencies, improving overall safety. To that end, this paper presents a novel Nonlinear MPC approach for vehicle control with deeply saturated rear tires. Longitudinal slip management is elevated from the chassis control layer into the optimisation problem by using a coupled-slip tire model, and explicitly including wheelspeed dynamics. Terminal costs on sideslip stability help compensate for the finite horizon, while road bounds and static obstacles are encoded using slack constraints. Experiments on a racetrack with a modified Toyota GR Supra validate the controller's ability to smoothly transition from dynamic, non-equilibrium drifting to grip driving. Further experiments demonstrate robustness to significant longitudinal force and wheelspeed disturbances, and showcase the controller flexibly transitioning in and out of the sliding tire regime to balance slack constraints with tracking objectives.

## ARTICLE HISTORY

Received 14 February 2023  
Revised 25 October 2023  
Accepted 28 November 2023

## KEYWORDS

Autonomous vehicles;  
chassis control systems;  
control; integrated control  
systems; nonlinear control;  
optimal control

## 1. Introduction

To truly scale to mass adoption and have a broad, positive effect, self-driving vehicles must be able to safely handle myriad different scenarios. Over many millions of miles, this will likely include edge cases where the vehicle may need to make a rapid, emergency maneuver. In the current paradigm, autonomous vehicle controllers are typically limited to operate only in conservative open loop stable conditions, as governed by existing underlying Electronic Stability Control (ESC) systems. While this may make the control problem simpler, it also greatly limits the achievable dynamic states of the vehicle. Indeed, expert drivers routinely utilise the increased agility enabled by operating with fully saturated rear tires, and do so while deftly balancing multiple other objectives [1]. Autonomous vehicle controllers that can operate similarly could access a much wider range of maneuvers, thus improving safety in many scenarios.

These expert examples have motivated the formal study of ‘drifting’ for vehicle control insights. The difficulty of driving in this regime arises from the fact that when the rear tires are fully sliding, yaw rate and sideslip become open-loop unstable [2]. Saddle operating

**CONTACT** Jonathan Y. M. Goh  [jonathan.goh@tri.global](mailto:jonathan.goh@tri.global)

 Supplemental data for this article can be accessed online at <http://dx.doi.org/10.1080/00423114.2023.2297799>.

© 2024 Toyota Research Institute. Published by Informa UK Limited, trading as Taylor & Francis Group. This is an Open Access article distributed under the terms of the Creative Commons Attribution-NonCommercial-NoDerivatives License (<http://creativecommons.org/licenses/by-nc-nd/4.0/>), which permits non-commercial re-use, distribution, and reproduction in any medium, provided the original work is properly cited, and is not altered, transformed, or built upon in any way. The terms on which this article has been published allow the posting of the Accepted Manuscript in a repository by the author(s) or with their consent.

points, corresponding to steady-state drifting, can be seen in various levels of vehicle model fidelity [3–5]. Adding further complexity, vehicle configuration and road surface conditions were shown to significantly impact minimum-time turn negotiation [6] and stability [7,8]. Several closed-loop control techniques have been used to stabilise the vehicle's dynamic states around a single equilibrium, including LQR [1,9], learning-based MPC [10], dynamic surface control [11], and reinforcement learning [12]. This requirement to stabilise the rotational states – absent in typical driving scenarios – implies that when adding on the additional task of tracking a path, there are more states than inputs, and the problem becomes underactuated. To address this, one approach used simplified dynamics to decompose steady-state drifting in a fixed circular orbit into sub-problems, tracking sideslip with bang-bang engine torque pulses, and heading with the steering actuator [13]. Another approach leveraged the nonlinear coupling between states that occurs when the rear tire is fully sliding, to show that by choosing to track vehicle position and sideslip with model inversion, vehicle velocity can be considered as an uncontrolled, but stable, zero dynamic [14]. This work experimentally demonstrated the importance of accounting for wheelspeed dynamics when operating at high tire slip, and was shown to generalise to slowly changing drifting equilibria, and then subsequently, also to rapid transitions between them [15].

By focussing on the specific challenges of autonomous drifting, these works have demonstrated insights for control in regions of very high tire slip. Extending these developments beyond their domain-specific assumptions to address more general driving tasks, however, remains a key challenge. A promising technique to achieve this is Nonlinear Model Predictive Control (NMPC), wherein the cost, dynamics, and constraints can be general nonlinear functions. Although the underlying vehicle model can have high fidelity for accuracy over a wide operating range, this needs to be balanced against convergence times and horizon length. Recently, several works have demonstrated the viability of NMPC for limit handling situations. By cascading models with decreasing complexity along the planning horizon, Laurence et al. demonstrated an NMPC approach for autonomous racing that balances near-term fidelity with longer horizon lengths [16]. A single-track representation with longitudinal weight transfer and non-linear tires was used as the short-range, highest fidelity model, and captured the dynamics well in experiments. By combining a similar model with a computationally efficient representation of the environment and ego vehicle in an NMPC framework, Brown et al. represented a scenario with a sudden vehicle cut-in [17]. In experimental testing, the controller was able to negotiate this emergency double lane change scenario in a combined braking and steering maneuver at the friction limits. The approach was further extended in [18] to include dynamic brake balance and online friction estimation. Other works on limit handling and emergency obstacle avoidance leveraged the flexibility of NMPC to explore varied concepts, including incorporating measures of uncertainty [19,20], moving obstacles in dynamic environments [21], and ensuring feasible contingency plans [22,23].

Taken together, these works suggest that leveraging the generalizability of NMPC with the design insights from drifting-specific approaches could yield a control framework that extends its operational domain to include the open-loop unstable, sliding tire regime. Such an approach could exhibit the agility of an expert driver to deftly execute an emergency maneuver, should an edge case situation require it. To that end, this paper presents a step towards this goal: an NMPC controller that can perform dynamic non-equilibrium



**Figure 1.** Photograph of ‘Keisuke’ test vehicle performing an autonomous drifting experiment on the Thunderhill West racetrack.

drifting, and also transition smoothly back to grip driving, while accounting for multiple objectives including road bounds. This approach is validated through several experiments on a full-size vehicle, including one on a racetrack (Figure 1).

As described in Section 2, one key feature of this framework is the choice of an isotropic coupled-slip model for the rear tires. Importantly, this model takes into account the coupling between longitudinal and lateral slip when the rear tire is fully sliding; indeed, beyond the saturation point, it is identical to the simplified fully-sliding-only model used successfully in [14]. To compute the longitudinal slip, driven rear axle wheelspeed is included as an explicit vehicle state in the NMPC problem formulation. This also allows the controller to compensate for real-time measurements of wheelspeed, rather than assuming a desired value as in a pure cascaded control approach [11,14]. As shown in experiments, this makes it practically robust to differences between the model and reality, as well as disturbances. Simple representations of wheelspeed and engine torque dynamics are also included, so the optimisation horizon can compensate for actuator delays as well as saturation of engine torque and engine torque slew rates.

The formulation of the NMPC controller is described in Section 3. To encode the task of drifting, we choose sideslip, path tracking error, and path angular deviation as reference tracking objectives; in a notable difference from typical driving scenarios, velocity is not included. To encourage smooth actuator responses – particularly engine RPM, which is highly apparent from both inside and outside the vehicle – these tracking objectives are balanced against action costs that include wheelspeed in addition to engine torque and steering angle slew rates. We expand the notion of path tracking from previous work in autonomous drifting to the more general task of staying within a prescribed boundary. To prevent feasibility issues when close to the edge, this is implemented as slack constraint using a large quadratic penalty on exceeding prescribed maximum/minimum bounds on lateral error that represent the available road area.

Finally, to help compensate for the finite length of the control horizon, a cost is added to represent sideslip stability at the terminal stage. This is formulated as a 2-norm penalty

on deviating from a first-order stable sideslip dynamic. This is inspired by the derivation of the controllability envelopes discussed in [15].

In Section 4, this approach is validated through experiments on a full-size Toyota GR Supra, ‘Keisuke’, that has been modified for high-performance and direct computer control of the actuators. The primary experiment consists of a slalom style drift trajectory performed on a commercial racetrack, specifically the West course at Thunderhill Raceway Park, Willows, CA. To foreshadow the concept of reacting to emergency situations, the NMPC controller is activated after a separate control sequence rapidly destabilises the car by applying brakes to lock-up the rear tires. At around 40 degrees of sideslip, the NMPC controller is activated, and thereafter fluidly transitions between two left and two right turn drifts using the full width of the track but staying within it, and avoiding obstacles encoded in the optimisation boundaries. The rear tires are fully sliding throughout this slalom drift sequence, and the vehicle achieves more than 55 degrees of peak sideslip, and more than 1.5 rad/s of peak yaw rate. After this sequence, the NMPC controller then smoothly returns the car to stable, straight-line grip driving, whereupon the experiment is ended.

The reliability and robustness of the controller and the fidelity of the chosen tire model are investigated by repeating the experiment several times. In a separate experiment to examine the response of the controller to external wheelspeed and longitudinal force disturbances, strong handbrake pulses, of which the controller is not aware, are manually injected by the safety driver during autonomous control. The results showcase the robustness of the approach, and highlight the importance of including the wheelspeed measurements and dynamics directly in the NMPC framework. In one exemplary instance, after a disturbance injection causes the rear tires to descend from high combined slip to levels below the sliding region, we subsequently see the controller purposefully re-enter the drifting state.

Indeed, these results point the way to control frameworks that can reliably extend their operating range beyond the point of tire saturation, potentially improving safety in emergency scenarios. In a departure from the current paradigm, this performance is in part unlocked by elevating wheelspeed and slip control away from single-purpose modules (e.g. ABS/ESC) and into the higher-level predictive controller. Subsuming these roles from proven production concepts, however, mandates a high level of responsibility; future work in this vein could investigate questions of reliability, in addition to further exploring the performance benefits.

## 2. Vehicle modelling

### 2.1. Choice of vehicle model and states

As shown in Figure 2, a single-track vehicle layout is used. We choose to use the yaw rate  $r$ , total velocity  $V$ , and sideslip  $\beta$  to represent the planar states of the vehicle. To locate the vehicle relative to the reference trajectory, we use a curvilinear (also known as Frenet) coordinate system. The position state of the vehicle is represented by the distance along the path,  $s$ , the lateral error from the path,  $e$ , and the angular deviation between the vehicle’s velocity vector and the path,  $\Delta\phi$ .

The vehicle is assumed to be rear-wheel drive. The steering angle,  $\delta$ , the rear axle wheelspeed,  $\omega_r$ , and engine torque,  $\tau$ , are included as explicit vehicle states. For this particular

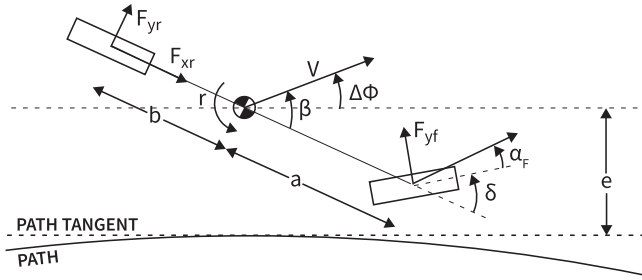


**Figure 2.** Single track bicycle model.

scenario, we choose to simplify the problem by assuming that brake torques are zero throughout the drifting phase, where throttle is applied and the rear tires are in positive longitudinal slip. It is hoped that this additional control surface will be explored in future work.

In total, there are eight vehicle states, with equations of motion:

$$\dot{x} = \begin{bmatrix} \dot{r} \\ \dot{V} \\ \dot{\beta} \\ \dot{e} \\ \dot{\Delta\phi} \\ \dot{\omega} \\ \dot{\delta} \\ \dot{\tau} \end{bmatrix} = \begin{bmatrix} \frac{aF_{yf}\cos(\delta) + aF_{xf}\sin(\delta) - bF_{yr}}{I_z} \\ \frac{-F_{yr}\sin(\delta - \beta) + F_{xf}\cos(\delta - \beta) + F_{yf}\sin(\beta) + F_{xr}\cos(\beta)}{m} \\ \dot{\phi} - r \\ V \sin \Delta\phi \\ \dot{\phi} - k_{ref} \frac{V \cos(\Delta\phi)}{1 - k_{ref}e} \\ \frac{G\tau - F_{xr}R}{I_w} \\ \dot{\delta} \\ \dot{\tau} \end{bmatrix} \quad (1)$$

Where  $a, b$  are the distances from the vehicle centre of gravity to the front and rear axles,  $m$  is the vehicle mass,  $G$  is the ratio from engine to wheel torque,  $R$  is the tire radius,  $I_z$  and  $I_w$  are the rotational inertia of the car and drivetrain, and  $k_{ref}$  is the curvature of the reference trajectory. Note that, for the specific vehicle drivetrain layout and problem specification explored in this paper, the front longitudinal force,  $F_{xf}$ , is assumed to be zero. The rate of change of the velocity vector direction,  $\dot{\phi}$  is:

$$\dot{\phi} = \frac{F_{yf}\cos(\delta - \beta) + F_{xf}\sin(\delta - \beta) + F_{yf}\cos\beta - F_{xr}\sin\beta}{mV} \quad (2)$$

The inputs to this vehicle model are then the steering angle slew rate,  $\dot{\delta}$ , and engine torque slew rate,  $\dot{\tau}$ :

$$u = \begin{bmatrix} \dot{\delta} \\ \dot{\tau} \end{bmatrix} \quad (3)$$

## 2.2. Tire modelling

During these high sideslip maneuvers, it is important to capture the impact of wheelspeed dynamics on the distribution between longitudinal and lateral forces; this motivates the use of a coupled slip tire model. Here, we assume an isotropic tire [24], such that the distribution between longitudinal and lateral tire force is the ratio of the respective slips to the total slip  $\sigma$ :

$$\begin{bmatrix} F_y \\ F_x \end{bmatrix} = F_{total} \begin{bmatrix} \frac{-\tan(\alpha)}{\sigma} \\ \frac{\kappa}{\sigma} \end{bmatrix} \quad (4)$$

where  $\alpha$  and  $\kappa$  are the lateral and longitudinal slip. These are computed from the single-track model vehicle states as:

$$\begin{aligned} \alpha_f &= \arctan \frac{V \sin(\beta) + ar}{V \cos(\beta)} - \delta \\ \kappa_f &= 0 \\ \alpha_r &= \arctan \frac{V \sin(\beta) - br}{V \cos \beta} \\ \kappa_r &= \frac{R\omega - V \cos \beta}{V \cos \beta} \end{aligned} \quad (5)$$

where <sub>f,r</sub> subscripts denote front and rear lumped tires. Note here the specific assumption that no longitudinal force is applied to the front wheels, so  $\kappa_f = 0$ .

The total force magnitude  $F_{total}$  is then created by the total slip  $\sigma$ , and we choose to use the Fiala brush model [25] to represent this relationship:

$$\begin{aligned} \sigma &= \sqrt{\tan(\alpha)^2 + \kappa^2} \\ \sigma_{sl} &= \arctan(3\mu F_z / C_f) \\ F_{total} &= \begin{cases} C_f \sigma - \frac{C_f^2 \sigma^2}{3\mu F_z} + \frac{C_f^3 \sigma^3}{27(\mu F_z)^2} & |\sigma| < \sigma_{sl} \\ \mu F_z & \sigma > \sigma_{sl} \end{cases} \end{aligned} \quad (6)$$

where  $C_f$  is the cornering stiffness, and  $\sigma_{sl}$  is the total combined slip at which the tire begins fully sliding. The Fiala brush model has been experimentally demonstrated for autonomous vehicle control at the limits of handling in numerous other works (e.g. [11,14,17]), and offers a blend of physical intuition, fidelity, and simplicity for computation.

Note that when the tire is fully saturated, this model corresponds exactly to the pure sliding tire assumption used in [14].

## 3. Controller design

### 3.1. Overview

In NMPC, a discrete optimal control problem is repeatedly solved for the states  $x_{0..N}$  and inputs  $u_{0..N}$  over the horizon of length  $N$ , by minimising a cost function  $J$ , described in

Section 3.5, subject to constraints:

$$\begin{aligned}
 & \min J \\
 \text{s.t. } & x_{k+1} = f(x_k, u_k, x_{k+1}, u_{k+1}) \quad \forall k \in [0, N-1] \\
 & x_0 = x_{\text{lookahead}} \\
 & x_{\min} \leq x_k \leq x_{\max} \quad \forall k \in [0, N] \\
 & u_{\min} \leq u_k \leq u_{\max} \quad \forall k \in [0, N] \\
 & \ddot{\delta}_{\min} < (\dot{\delta}_{k+1} - \dot{\delta}_k) \dot{s}_k < \ddot{\delta}_{\max} \quad \forall k \in [0, N-1]
 \end{aligned} \tag{7}$$

This problem is firstly subject to the discretised dynamics transition between each stage Section 3.2, with the initial state constrained to be equal to  $x_{\text{lookahead}}$ , a short-range forecast of the current vehicle state Section 3.3. Thereafter, constraints on the physical actuators Section 3.4 are expressed as a combination of inequality box constraints on  $x$ ,  $u$ , and an approximation for the steering angle acceleration.

### 3.2. Discretization of dynamics

The reference trajectory is encoded as a function of the distance along the curvilinear path,  $s$ . To facilitate having a static reference horizon for the MPC optimisation problem, it is thus convenient to express the dynamics (1) in spatial terms along the reference trajectory:

$$\begin{aligned}
 \frac{dx}{ds} &= \frac{dx}{dt} \left( \frac{ds}{dt} \right)^{-1} \\
 &= \dot{x} \left( \frac{V \cos \Delta\phi}{1 - k_{\text{ref}} e} \right)^{-1}
 \end{aligned} \tag{8}$$

These spatial dynamics are then discretised using an implicit RK2 scheme, which has been shown by other works, e.g. [19], to provide a good balance between fidelity and computation time, even in highly dynamic scenarios.

$$\begin{aligned}
 x_{k+1} &= f(x_k, u_k, x_{k+1}, u_{k+1}) \\
 &= x_k + \frac{ds_k}{2} \left( \frac{dx}{ds}(x_k, u_k) + \frac{dx}{ds}(x_{k+1}, u_{k+1}) \right)
 \end{aligned} \tag{9}$$

where  $ds_k$  is the path distance step length at the  $k$ -th step. We use  $N_S = 5$  short steps, each of length  $ds_S = 0.75$  m, at the start of the horizon to accurately capture the dynamics in the near-term. Subsequently, there are  $N_L = 15$  long steps, each of length  $ds_L = 3$  m, to forecast further along the path. In total, there are  $N = N_S + N_L = 20$  control intervals, for a total horizon length of 48.75 m.

### 3.3. Initial state constraint

The optimisation problem takes some non-trivial time to solve, usually below  $t_{\text{opt}} = 50$  ms. For the high dynamic rates seen in this kind of maneuver, the states can change appreciably

in that time. To compensate for this delay,  $x_{lookahead}$  is computed by forward integrating the measured states of the vehicle.

The states  $x_{init}$  at the start of the integration are a combination of measured vehicle states, and input states from the previous solution:

$$x_{init} = \begin{bmatrix} r_{meas} \\ V_{meas} \\ \beta_{meas} \\ e_{meas} \\ \Delta\phi_{meas} \\ \omega_{meas,proj} \\ \delta_{prevsol} \\ \tau_{prevsol} \end{bmatrix} \quad (10)$$

where the subscript  $meas$  refers to measured values, and the subscript  $prevsol$  refers to values from the previous optimal solution, interpolated at the current distance along the reference path. The subscript  $proj$  refers to states that are projected to be within optimisation constraints, if necessary.

To compute  $x_{lookahead}$ , this initial state is then propagated forward by  $t_{opt}$  through the model (1); at each integration step, the input values  $\delta_{prevsol}$ ,  $\tau_{prevsol}$  are interpolated from the previous solution.

### 3.4. Actuator constraints

To enable rapid vehicle movement (e.g. during dynamic drifting transitions), without losing control authority, it is important to account for the saturation and dynamics of the actuators. The steering angle state is simply limited by the range of the steering rack movement, while the engine limits are approximated as constant bounds on torque and wheelspeed:

$$\begin{bmatrix} \delta_{min} \\ \omega_{r,min} \\ \tau_{min} \end{bmatrix} \leq \begin{bmatrix} \delta \\ \omega_r \\ \tau \end{bmatrix} \leq \begin{bmatrix} \delta_{max} \\ \omega_{r,max} \\ \tau_{max} \end{bmatrix} \quad (11)$$

The input slew rates are also constrained to physically realisable values:

$$\begin{bmatrix} \dot{\delta}_{min} \\ \dot{\tau}_{min} \end{bmatrix} \leq \begin{bmatrix} \dot{\delta} \\ \dot{\tau} \end{bmatrix} \leq \begin{bmatrix} \dot{\delta}_{max} \\ \dot{\tau}_{max} \end{bmatrix} \quad (12)$$

Finally, to approximate the acceleration limits of the steering actuator without introducing another state to the formulation, the finite difference of the steering angle slew rate, after conversion to a temporal basis, is constrained:

$$\ddot{\delta}_{min} < (\dot{\delta}_{k+1} - \dot{\delta}_k)\dot{\tau}_k < \ddot{\delta}_{max} \quad (13)$$

The risk of infeasibility from these constraints is eliminated during initial state propagation Section 3.3 by a) taking steering and engine torque from the previous optimal solution, and b) projecting the measured wheelspeed to be within  $\omega_{r,min}$  and  $\omega_{r,max}$ .

### 3.5. Cost function formulation

The cost function  $J$  is formulated to optimally balance several objectives:

$$J = J_T + \sum_{i=0}^N (J_{Q_i} + J_{R_i} + J_{S_i}) \cdot ds_i \quad (14)$$

The primary tracking cost  $J_Q$  is balanced against the primary actuator cost  $J_R$ . These alone, however, do not adequately capture the importance of staying on the track, which is encoded by the slack cost  $J_S$ . These running costs are accumulated over the horizon, and weighted by the length of each step  $ds$ . The second-level subscript  $i$  notates evaluation at that stage.

Finally, the terminal stability cost  $J_T$  helps to compensate for the finite length of the control horizon.

#### 3.5.1. Primary running costs

We formulate the primary tracking cost  $J_Q$  as a weighted sum of reference sideslip, lateral error and course error:

$$J_Q = [Q_e \quad Q_\beta \quad Q_{\Delta\phi}] \begin{bmatrix} e^2 \\ \beta_{rel}^2 \\ \Delta\phi^2 \end{bmatrix} \quad (15)$$

where for compactness we introduce the subscript  $rel$  to refer to quantities relative to the reference trajectory:

$$\gamma_{rel} = \gamma - \gamma_{ref} \quad (16)$$

This is similar to the choice of objectives in the model inversion controller presented in [14]; as discussed there, although vehicle velocity is not explicitly tracked in the objective function, we expect it to be stable around the reference velocity due to the coupling between dynamic states when the rear tires are operating in the fully sliding region.

The selection of actuator costs  $J_R$  shapes the response of the controller to disturbances. To encourage general input smoothness, we directly penalise the trajectory-relative magnitude of the input slew rates. Inspired by the sport of professional drifting, where a consistent and smooth engine sound is an important factor, we also place a relatively large cost on trajectory-relative deviations in wheelspeed, but no cost on steering angle. Both in simulation and in experiments (not reported here), it was observed that decreasing this cost caused the controller to prefer larger steering corrections and less wheelspeed corrections, and vice-versa.

Finally, to aid convergence when the gradient of the tire force curve is zero, a small regularisation cost is added to the front slip angle, similar to the technique described in [16].

$$J_R = [R_t \quad R_\delta \quad R_\omega \quad R_\alpha] \begin{bmatrix} \dot{\tau}_{rel}^2 \\ \dot{\delta}_{rel}^2 \\ \omega_{rel}^2 \\ \alpha_f^2 \end{bmatrix} \quad (17)$$

### 3.5.2. Track bound violations slack cost

To prevent feasibility issues if the vehicle temporarily exceeds track boundaries, we encode the track boundaries as a heavily penalised slack constraint:

$$J_S = W_S db(e, e_{min}, e_{max})^2$$

$$db(e, e_{min}, e_{max}) = \begin{cases} e - e_{min} & e < e_{min} \\ e - e_{max} & e > e_{max} \\ 0 & \text{otherwise} \end{cases} \quad (18)$$

where  $e_{min}, e_{max}$  refer to the minimum and maximum allowable lateral error, encoding the boundaries in curvilinear (Frenet) coordinates.  $W_S$  is the large slack cost weight, and the function  $db$  is a deadband-like function that is zero if the vehicle is within the boundaries. This formulation is similar to that used for a straight tube in [17], but reformulated for a generalised curvilinear co-ordinate system. Note that the weight  $W_S$  is adjusted to be much larger than  $Q_e$ , the cost on lateral error described in 3.5.1. Together, these costs shape the penalty function on lateral error such that deviating from the reference path is relatively cheap until the track boundary is exceeded, where it increases massively.

### 3.5.3. Terminal stability costs

To compensate for the finite length of the control horizon, a cost is added to represent sideslip and lateral error stability at the terminal stage. Stable first-order desired dynamics can be represented as:

$$\begin{aligned} \dot{\beta}_{des} &= -k_\beta \beta_{rel} \\ \dot{e}_{des} &= -k_e e \end{aligned} \quad (19)$$

where  $k_{beta}, k_e$  are time constants. A quadratic penalty is then imposed on deviating from these dynamics at the terminal stage (notated as subscript  $F$ ):

$$J_T = \begin{bmatrix} V_{\dot{\beta}_F} & V_{\dot{e}_F} \end{bmatrix} \begin{bmatrix} (\dot{\beta}_F - \dot{\beta}_{des})^2 \\ (\dot{e}_F - \dot{e}_{des})^2 \end{bmatrix} \quad (20)$$

Similar to the other costs, the weights on these stability constraints were tuned by hand with the aid of closed-loop simulations, and were observed to have a significant effect; a detailed examination and sensitivity analysis of this and other parameters is not included in this paper, but could be interesting for future study.

## 3.6. Solver implementation details

For development flexibility and ease of implementation, the optimal control problem is posed using the CasADi [26] auto-differentiation and code-generation toolbox. The generated problems are then subsequently solved online with the IPOPT [27] interior point solver. If available, the initial guess for each solve is set to the previous converged optimal solution. Otherwise, it is set to a trivial zero-order-hold guess, i.e. where the initial states are held constant across the horizon. To prevent runaway computation, the solver is constrained to use a maximum of 50 iterations; when the limit is hit, the current solve attempt



**Figure 3.** Photograph of ‘Keisuke’, the modified Toyota GR Supra test vehicle that was used for experimental validation.

is aborted and the latest optimisation problem is started instead. CasADi and IPOPT were also used for the offline planning of the reference trajectories Section 4.2.

## 4. Experimental validation

### 4.1. Experimental vehicle platform

This approach was tested on ‘Keisuke’ (Figure 3), a Toyota GR Supra that has been customised for autonomous driving research. Because one of the other purposes of this platform is to obtain data from professional motorsports drivers, it has also been modified to be similar to vehicles used in the ‘Formula Drift’ competition [28].

Engine modifications include a larger turbocharger, custom intake and exhaust, as well as bespoke control/management software that is configured to allow direct computer actuation of the throttle plate angle. It is also equipped with a manual sequential transmission and clutch that can be computer controlled via custom pneumatic and hydraulic systems, respectively. The aftermarket suspension is similar to that used by many professional drifting teams, with more caster angle and a wider steering range. A motor on the steering column allows for by-wire operation in tandem with the hydraulic power assist rack. The primary braking system allows for fast, individual control of pressure on all four corners. A secondary handbrake system that only affects the rear wheels is connected using an isolated hydraulic circuit with separate master cylinder, lines, and callipers.

Vehicle state information, including position, velocity, and sideslip, is obtained from a dual-antenna RTK-GNSS-aided INS system (Oxford Technical Systems RT3003) at a rate

of 250 Hz. The NMPC optimisation problem is computed on an x86-based PC, equipped with an Intel Xeon E-2278GE (base frequency 3.30 GHz) and running Ubuntu Linux. When complete, the solution is sent via network to a hard real-time computer (dSpace MicroAutoBox II).

At 10 ms intervals, engine torque and steering angle commands are computed by interpolating into the current optimisation solution based on the position of the vehicle relative to the reference path. In turn, these commands are cascaded into low-level closed-loop control, running at 5 ms timesteps, to arrive at final actuator values for the steering motor current and throttle plate angle. While steering angle control is straightforward, it should be noted that, due to the aftermarket modified nature of the vehicle, engine torque control depends on empirically estimated lookup tables for the relation between manifold pressure and engine torque, as well as the relation between flow rate, turbocharger RPM, turbocharger pressure and manifold pressure; this leads to considerable uncertainty in the identified engine dynamics and reported estimates of engine torque.

## 4.2. Experimental procedure

### 4.2.1. Primary scenario: drift slalom on racetrack

The primary experiments were conducted on the ‘West Track’ of Thunderhill Raceway Park in Willows, California, USA. As illustrated in Figure 5, this scenario consists of three sections: initial grip driving (blue), handbrake destabilisation (orange), and transient drifting (green). The NMPC controller is started immediately after the handbrake destabilisation section, and is responsible for controlling the vehicle through the transient drifting section, and back to grip driving afterwards; this section is the primary focus of this paper. The grip driving and handbrake destabilisation stages are controlled using separate, non-MPC controllers. For brevity, the details of these controllers are not included here, and the trajectory planning procedure is only briefly described.

The reference trajectory is computed offline using a multi-stage nonlinear optimisation routine with the same vehicle model. To ensure some margin for closed-loop control, all sections are constrained to stay above a minimum distance from the edges of the track. To better reflect the complexity and non-smoothness of a real-world scenario where other objects may be present on the road, several static obstacles are included as sharp perturbations in this envelope. The NMPC controller uses this same envelope for the road bounds slack constraint described in Section 3.5.2.

Each section is computed separately, and are tied together with initial / final state constraints that are selected by hand as design choices. The grip driving section starts in a straight ahead driving state, with zero yaw rate and sideslip, and ends in a stable turning equilibrium. Subsequently, the handbrake destabilisation sequence rapidly transfers the vehicle from this stable equilibrium to a drifting equilibrium, subject to a zero wheel-speed constraint on an interior subset of the trajectory. Although it is possible to transition from grip driving to drifting using the NMPC controller alone, this initiation method was selected to more closely resemble an emergency situation: a vehicle is suddenly thrown into instability, and already at high yaw rate and sideslip when the controller has to turn on, start solving from a cold start, and produce actuator commands that prevent it from leaving the road.

The transient drifting section begins at this drifting equilibrium, and ends in a straight ahead driving state. Several points along the trajectory are constrained to have a given sideslip; these are selected by hand as design choices. To ensure that the controller has headroom for real-time control, the actuator slew rate limits are specified as strictly lower than that used in the NMPC controller. Finally, to enforce that this section is one continuous drifting sequence, the longitudinal slip of the rear tires is constrained to be above a minimum value until the exit of the final corner.

#### **4.2.2. Secondary scenario: Figure 8 on skidpad**

The secondary scenario is a Figure 8 trajectory (Figure 12) on a large skidpad. The NMPC drifting section is composed of steady-state arcs connected by rapid transitions. Similar to the primary scenario, grip driving and handbrake destabilisation stages precede this section.

#### **4.3. Primary experimental results**

In Figure 4, a composite photo superimposes stills from an overhead video of a test at 0.5 s intervals, showing the path and pose of the car throughout the closed-loop trajectory. This video, and two other drone videos of representative experimental runs, are included as Supplementary Material. A more quantitative version of this overview is synthesised from the measured poses of the vehicle, as shown in Figure 5. The reference path and specified bounds are also shown. To capture the dynamic nature of these maneuvers, a video of these experiments from several perspectives can be found at [https://www.youtube.com/watch?v=MfU5\\_gzqPaM](https://www.youtube.com/watch?v=MfU5_gzqPaM).

The measured states of the vehicle are shown in Figure 6. At  $s \approx 85$  m, the handbrake destabilisation stage activates, and maximum pressure is applied to the rear brakes, while



**Figure 4.** Composite photo superimposing stills from an overhead video of a test at 0.5 s intervals.

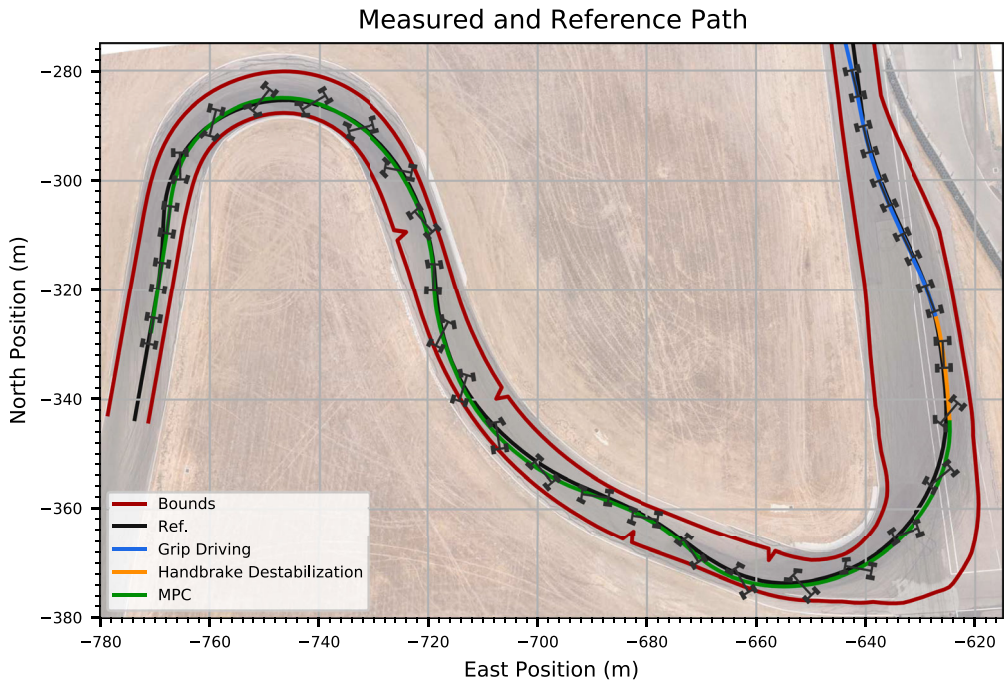


**Figure 5.** Measured and reference path of the vehicle during experimental run. The pose of the vehicle is also shown at regular intervals. Note that the schematic vehicle is scaled by 200% for clarity.

simultaneously, the clutch is hydraulically disengaged. We see the measured wheelspeed (blue line, fourth plot from top) quickly drop to zero. Yaw rate rapidly decreases, reaching a peak of  $\sim -1.2$  rad/s, which in turn causes sideslip to rapidly rise. Counter-steering is quickly applied, and steering angle switches sign from slightly negative to near saturation in the positive direction. This maneuver takes less than  $\sim 1.2$ s, or, as visualised in Figures 4 and 5, about five car lengths. At the end of this stage ( $s \approx 100$  m), the rear brakes are released, the clutch is engaged, and wheelspeed very rapidly rises to match the engine speed. Simultaneously, the NMPC controller is turned on, and begins to solve the first optimisation problem. Approximately 50 ms later, upon successful convergence, at a sideslip of  $\approx 0.7$  rad, and a yaw rate of  $\approx -0.5$  rad/s – well into the open-loop unstable region – control is handed off, and the NMPC stage begins.

Throughout this NMPC stage, highlighted in green (Figure 6), the controller showed overall good performance: it kept the vehicle within the prescribed track bounds, while tracking the control objectives – sideslip, lateral error, and path angular deviation – with smooth inputs. The rear tires are fully sliding throughout this slalom drift sequence, and the vehicle achieves more than  $\sim 55$  degrees of peak sideslip, and more than  $\sim 1.5$  rad/s of peak yaw rate.

As with any MPC approach, the desired controller behaviour can be adjusted by tuning the relative costs; the effects of our particular gain set can be seen in different trade-offs during the trajectory. Within the tracking objectives  $J_T$ , a relatively high cost was placed on sideslip, resulting in good tracking of the reference, as reflected in the third subplot. In professional drifting, having a consistent engine note is an important aesthetic factor, and

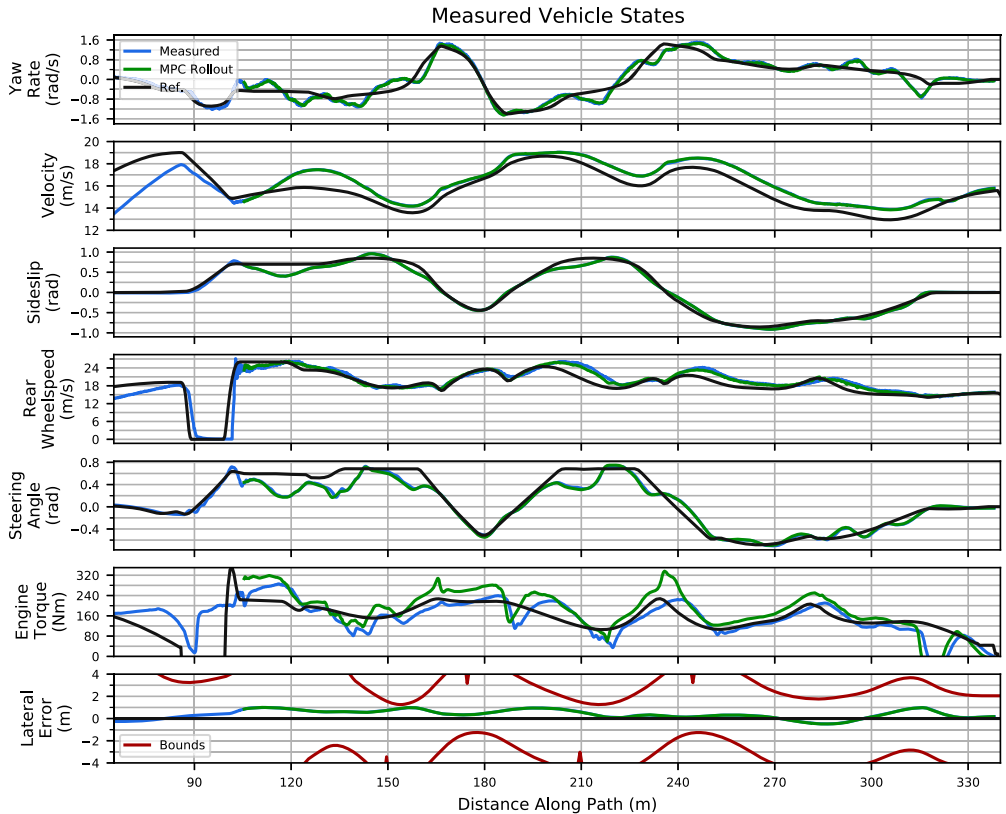


**Figure 6.** Measured vehicle states during an experimental run.

this motivated placing a larger relative cost on rear wheelspeed compared to the other actuator cost terms (Equation (17)). This results in a very smooth wheelspeed signal (fourth subplot), and in general the controller prefers to use the steering actuator, except when steering alone cannot adequately compensate for tracking errors. For example, at  $s = 210$  and  $s = 240$  m, we see the controller add bigger sacrifices in wheelspeed, on top of large steering angle deviations, in order to deepen the drift and catch up to the reference sideslip. As it makes these real-time adjustments, the controller is free to let vehicle velocity vary, as it is not included as a tracking objective. We see this reflected in the second plot, where the measured velocity strays quite far from the reference.

Lastly, this performance is achieved despite considerable uncertainty between the estimated engine torque and the commanded signal, as seen in the last plot. One possible explanation for this robustness is in the direct use of the wheelspeed measurements in the NMPC controller, so that it can compensate for the actual – rather than desired – values of longitudinal slip; this is examined further in Section 4.5.

The lateral error is shown in the last subplot, along with the prescribed boundaries (red). While the cost on tracking lateral error is relatively small, the slack cost for track bound variation is necessarily very large. The effect of this weighting can be seen by comparing two regions on the trajectory. At  $s = 110$  m, the wheelspeed is near its upper limit, and steering is the only available bidirectional actuator. Since the vehicle is far from the boundary, we

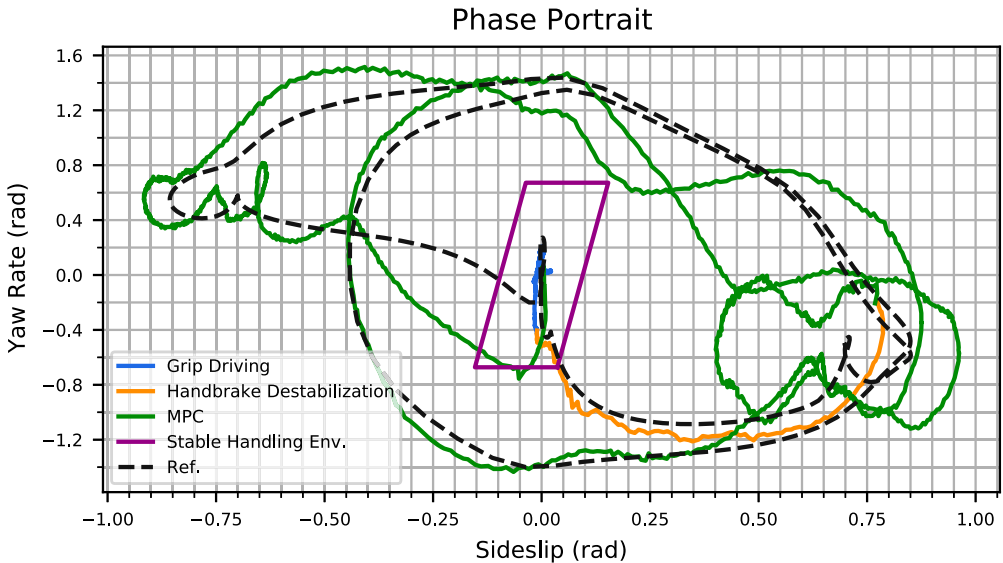


**Figure 7.** Measured and planned sideslip-yaw rate phase portrait during an experimental run.

see it leaving lateral error at a steady, non-zero value, while it uses steering movements to temporarily raise yaw rate and smoothly increase sideslip. This contrasts with  $s = 155$  m, where the vehicle is very near the track boundary, and the controller appears to sacrifice sideslip tracking in order to prevent exceeding it.

As a complement to this time series data, another illuminating way to view this result is in the sideslip-yaw rate phase plane, as depicted in Figure 7. Also shown is the ‘stable handling envelope’, as defined by [29], computed at the start of the NMPC stage. The vertical lines of this envelope correspond to saturation of the rear tire, and the horizontal lines represent an approximation of the maximum steady-state yaw rate; this envelope thus represents an intuitive visual estimate (albeit a conservative one [30]) to the guaranteed stable region of the phase plane. The measured data starts well within this envelope in the grip driving stage (blue), then is rapidly taken outside these bounds during the handbrake destabilisation stage (orange). Thereafter, the NMPC controller (green) guides the vehicle throughout the phase plane in a fluid, non-equilibrium manner, smoothly changing directions while fully exploiting states with high yaw rate and sideslip – all while simultaneously keeping the car within the bounds of the road. It then takes the vehicle back to grip driving within the stable region, after which the experiment is ended. Indeed, viewing the data on this phase plane starkly illustrates how much more yaw rate and sideslip can be achieved when not constrained to operate within the stable handling envelope.

#### 4.4. Insights from repeated testing

##### 4.4.1. Performance analysis

To investigate robustness and reliability, this experiment was repeated  $n_{tests} = 13$  times, all in one session. Because the same set of tires are used throughout these runs, it is expected

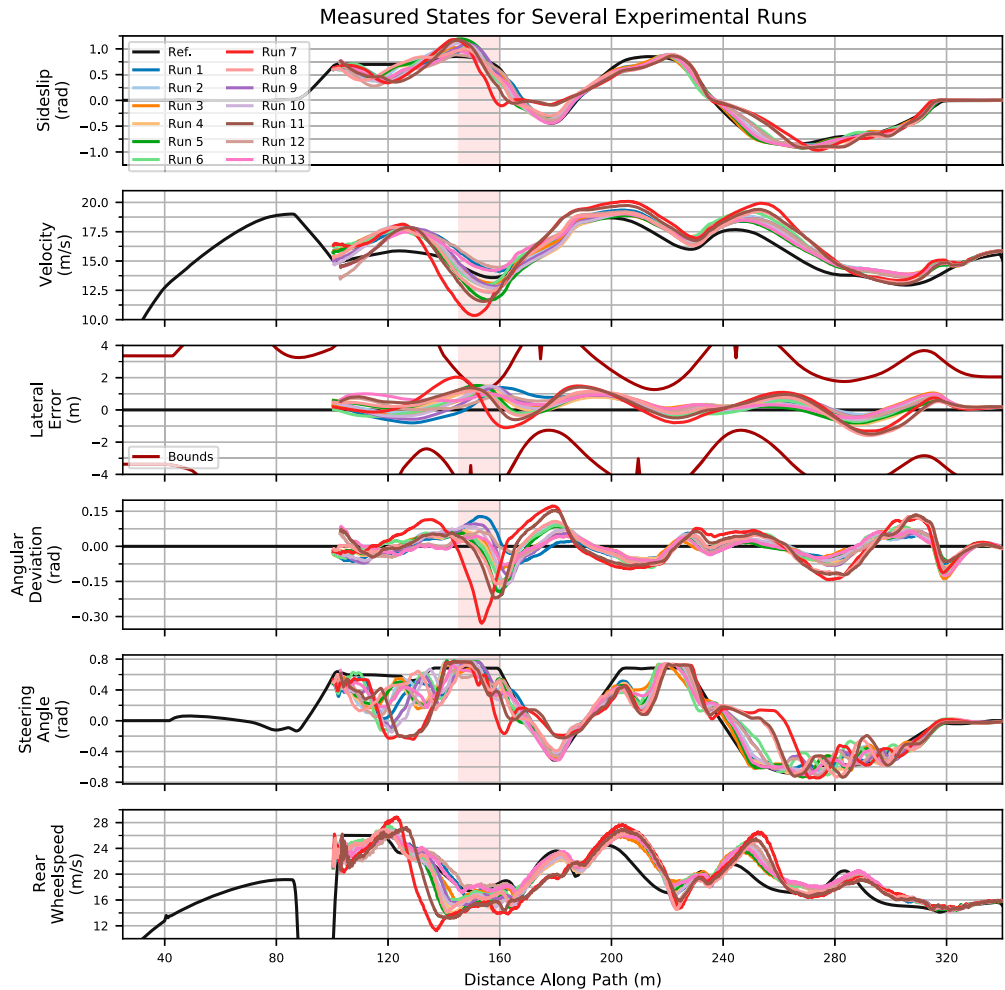


**Figure 8.** Measured vehicle states for 13 experimental runs. The red highlighted area shows the section of the runs in which the vehicle comes closest to the edge of prescribed bounds, and corresponds to the red histograms in Figure 9.

that the considerable tire wear and temperature variation could introduce significant variability to the observed vehicle behaviour. Figure 8 shows selected states, namely sideslip, velocity, lateral error, steering angle and rear wheelspeed, for each of these runs. To qualitatively illustrate the similarities and differences between tests, a video overlaying two representative runs is available as Supplementary Material.

The handbrake destabilisation stage introduces a large range of initial conditions, especially in velocity and path angular deviation. Overall, the results of these runs look qualitatively similar. Although the general trend of the reference trajectory is accomplished, runs 7 (dark red), 8 (light red), and 11 (dark brown) appear to stand out for having significantly larger sideslip tracking error than the rest. Run 7, which has the largest deviations, as seen at  $s \approx 160$  m and  $s \approx 250$  m, is interesting to examine as the ‘worst’ case observed in this set of experiments. At  $s \approx 140$  m, we see a rapid rise in lateral error, quickly approaching the

boundary. To prevent leaving the track, the controller subsequently drops wheelspeed and sacrifices sideslip tracking. In fact, sideslip drops to near zero, indicating an exit from the sliding rear tire condition from  $s \approx 160$  m to  $s \approx 175$  m. After this, we see the controller re-initiate the drift, while continuing to stay on the path; this indicates the controller's ability to operate in both grip and saturated tire conditions, and transition between them as needed. A lag in sideslip evolution at the transition at  $s \approx 230$  m is compensated with a large steering deviation into the turn, after which the behaviour is similar to the bulk of the other runs.

While 8 of these runs stayed within the bounds, 5 of them exceeded the bounds at some point. Of the runs that exceeded the bounds, the maximum lateral error violation was 0.24 m, while the mean was 0.16 m. These track bound violations occur at the first turn of the trajectory, right after the uncertainty introduced by the rapid handbrake initialisation. Because the track bounds are encoded as soft constraints (Equation (18)), the controller continues to be feasible and produce solutions that bring the vehicle away from the bounds, while trading off other tracking objectives.

The measured density distribution of lateral error, accumulated over the entire NMPC stage for all runs, is shown in teal on the left side of Figure 9. We see an overall symmetric shape, centred near zero, consistent with a symmetric, squared error tracking objective in the presence of uncertainty. The red histogram shows the lateral error for the 15 m section of the runs near the closest point of approach to the track boundary, within which all the track violations occur, as illustrated in Figure 8. In contrast to the overall behaviour, we see a decidedly asymmetric distribution, indicating the activation of the track boundary soft constraint. The purple line indicates the average maximum boundary location,  $e_{max}$ , over the section and corresponds to a steep falloff in probability density. Accompanying this, on the right side of Figure 9, we see a much wider range of sideslip values over this section

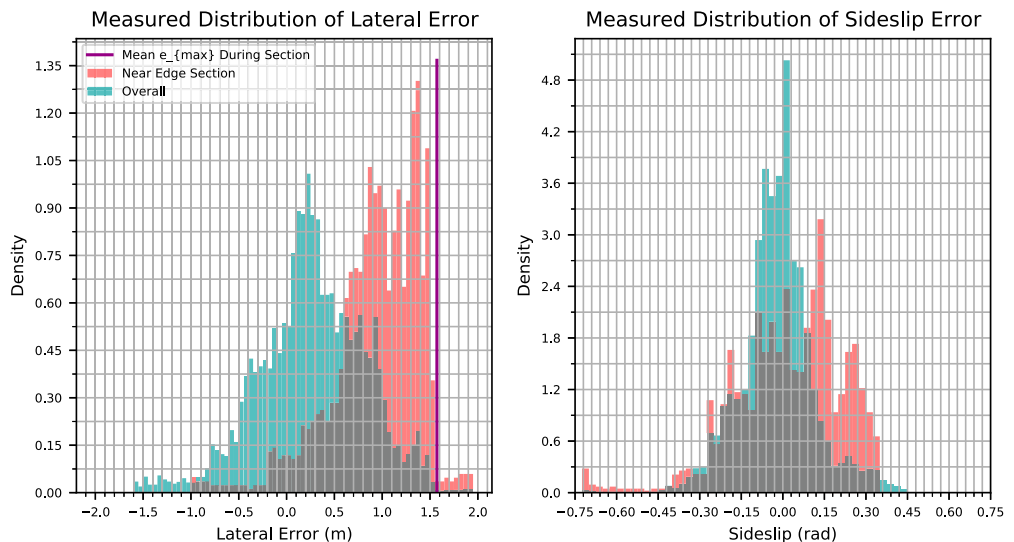


**Figure 9.** Measured distribution of lateral error and sideslip reference tracking error. The teal histogram shows measurements accumulated over the NMPC stages of all runs. The red histogram shows the section of the runs, highlighted in Figure 8, in which the vehicle comes closest to the prescribed bounds.

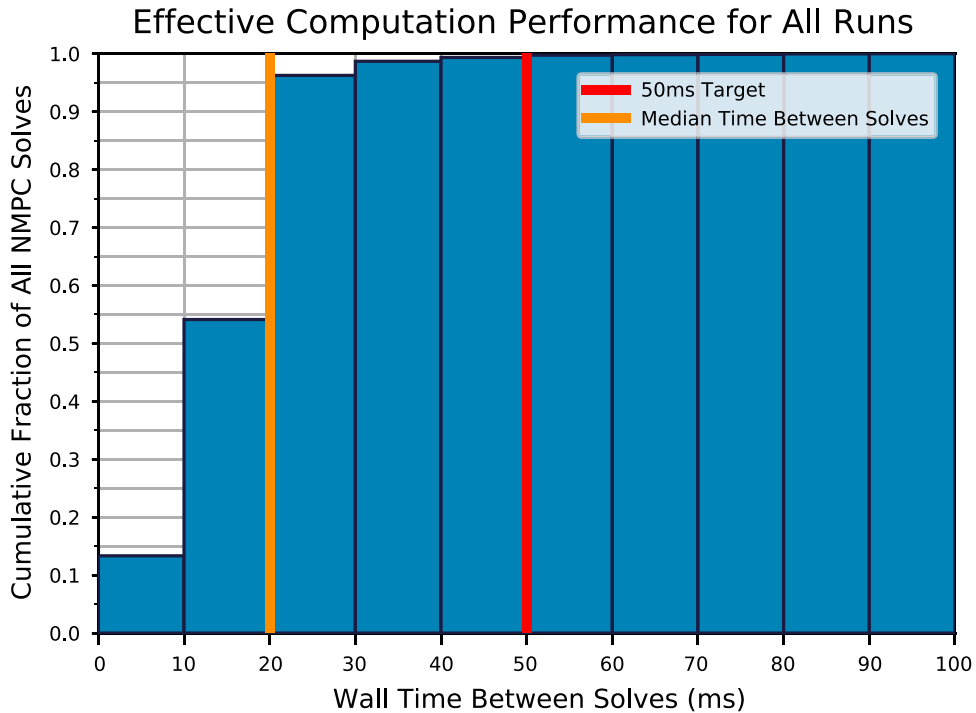


**Figure 10.** Measured cumulative distribution of wall time between solves, aggregated for all runs.

(red) than during the overall trajectory (teal), suggesting that this soft constraint activation is concomitant with a trade-off in increased sideslip tracking error.

#### 4.4.2. Computation time

To evaluate the effective computation performance, we use the time between solutions received on the hard real time computer. Because this computer runs at a fixed 100 Hz frequency, this metric is quantised in 10 ms increments. While the time to solve the optimisation problem dominates this number, it also includes other necessary tasks, e.g. sending the solution over the network, and interpolating into the solution.

Across these runs, the optimisation problem was solved a total of 10,889 times. Of these, 99.4% were within the design budget of 50 ms; that is, the allotted time was exceeded on only 67 occasions. This is also visualised in Figure 10, which depicts the measured cumulative distribution of this time-between-solves metric, aggregated for all runs. The median solve time was 20 ms. Overall, the computation performance suggests that such an approach is practically realisable for real-time applications, even with readily available off-the-shelf computer hardware.

#### 4.4.3. Tire model validation

The repetition of these tests presents an opportunity to examine tire forces on a real car across a very wide range of slips. Since no front brakes are applied during the experiment, we can assume front longitudinal force is zero, and the remaining three forces for the single-track model can be estimated from measurements of the vehicle state derivatives  $r$ ,  $V$ ,  $\beta$  by

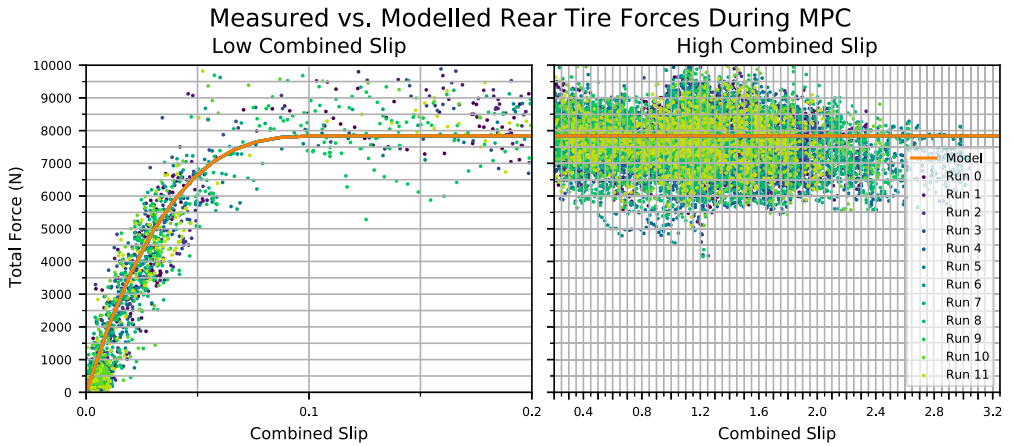


**Figure 11.** Measured and modelled rear tire forces over several experimental runs on the slalom trajectory.

inverting the equations of motion in (1):

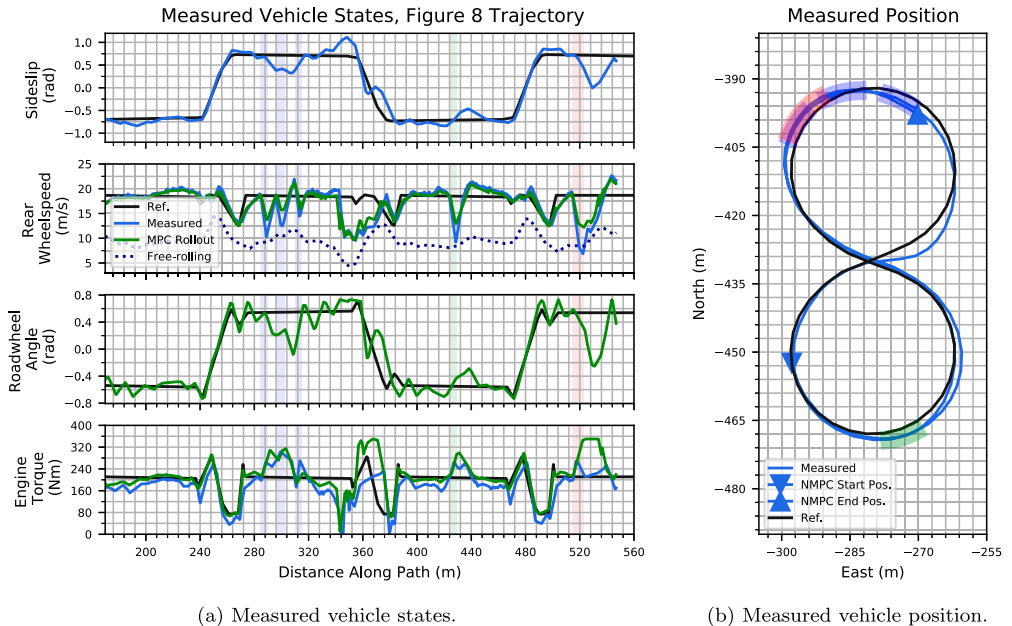
$$\begin{bmatrix} \bar{F}_{yf} \\ \bar{F}_{xr} \\ \bar{F}_{yr} \end{bmatrix} = \begin{bmatrix} \frac{a \cos \delta}{I_z} & 0 & \frac{-b}{I_z} \\ \frac{-\sin(\delta - \beta)}{m} & \frac{\cos \beta}{m} & \frac{\sin \beta}{m} \\ \frac{\cos(\delta - \beta)}{mV} & \frac{-\sin \beta}{mV} & \frac{\cos \beta}{mV} \end{bmatrix}^{-1} \begin{bmatrix} \dot{r} \\ \dot{V} \\ \dot{\beta} \end{bmatrix} \quad (21)$$

Figure 11 depicts the estimated total rear force,  $\bar{F}_{r,\text{total}} = \sqrt{\bar{F}_{xr}^2 + \bar{F}_{yr}^2}$ , measured during these runs against the combined rear tire slip  $\sigma$ . The modelled rear tire force (2.2) is shown as an orange line, and suggests a generally good fit – especially given the simplicity of the formulation – in both the low saturation ( $\sigma < 0.2$ , left subplot), and high saturation ( $0.2 < \sigma < 3.2$ , right subplot) regions. This suggests that the selected isotropic combined tire slip model offers a good compromise between computational complexity and effectiveness for control.

Examining this figure also suggests a few features that may be better captured by a more complex representation. Firstly, there appears to be a falloff in total force at very high combined slips ( $\sigma > 2.0$ ), suggesting a two-friction brush model could be more appropriate. Secondly, there is considerable scatter at the transitional region ( $\sigma \approx 0.75$ ), likely attributable to unmodelled effects (e.g. weight transfer), and limitations with the isotropic assumption. Lastly, capturing variations in normal load would likely improve accuracy throughout. While these modifications could improve fidelity, they would likely also come at the expense of increased computational load, especially in the context of MPC.

#### 4.5. Secondary experimental results: disturbance injection testing

One important aspect of control during high-slip maneuvers that is not present during normal driving situations is the significance of wheelspeed dynamics; this motivated incorporating wheelspeed dynamics directly into the NMPC approach. To evaluate robustness to disturbances, we injected external braking forces on the rear tire during an autonomous



**Figure 12.** Measured vehicle states and position during disturbance injection experiments on a ‘Figure 8’ trajectory. Coloured boxes highlight sections where large handbrake pressure was manually added by the safety driver. (a) Measured vehicle states and (b) Measured vehicle position.

test. This was accomplished by the safety driver using a manually operated handbrake that has an independent hydraulic setup Section 4.1.

To ensure safety, experiments were conducted on a large skidpad rather than the race course. A symmetric ‘Figure 8’ trajectory (Figure 12), with constant-radius sections connected by rapid transitions, was used as the reference path. A similar handbrake destabilisation sequence was used to start the drift.

Measured and reference vehicle states during the NMPC section of the test are shown on the left side of Figure 12, and the measured and reference vehicle paths are shown on the right. During the first constant-radius section, the handbrake is not activated. This benchmark response shows smooth steering, wheelspeed, sideslip and engine torque responses that are close to the reference. For both plots, the light blue, light green, and light red shapes highlight parts of the second, third, and fourth constant-radius sections during which the safety driver pulled the handbrake.

The controller’s predicted wheelspeed rollout (green), is the measured initial state propagated forward in time firstly by the previous solution’s input values Section 3.3, and subsequently by the optimal solution that is followed for at least  $t_{opt} = 50$  ms or until the next solve is available. Thus, we see that during periods of handbrake application, it broadly follows the downward trend due to the initial state constraint, but fails to capture the full magnitude of the slope due to propagating dynamics that neglect the presence of this disturbance force. Yet, in each instance, we see the controller respond largely appropriately, by rapidly steering into the turn and applying additional engine torque to help improve sideslip while maintaining path tracking. Overall, the controller appears broadly robust to these very large disturbances, and continues to solve smoothly.

The last application of handbrake, shown in red, is of an extended duration, and leads to particularly interesting behaviour. Here, the wheelspeed slows to below the free-rolling speed, and sideslip drops to approximately zero. That is, the vehicle drops out of the fully-sliding region completely, and into typical grip driving conditions. After the handbrake is released, the controller responds by saturating the demanded engine torque and sharply steering into the turn, thereby bringing the car back into the drift. This example highlights the ability of the controller to operate in a wide range of conditions, at both low and high tire slip, and transition between them as needed.

## 5. Conclusion

This paper presents a Nonlinear Model Predictive Control (NMPC) approach for vehicle control that extends into the open-loop unstable sliding tire regime, as manifest in the task of automated drifting.

To capture the most important vehicle dynamics effects, while balancing computational complexity, we choose a nonlinear single-track model with an isotropic coupled-slip rear tire, and also explicitly include wheelspeed and engine torque dynamics. The tracking objectives of sideslip, lateral error, and path angular deviation are balanced against the smoothness of wheelspeed and the engine torque and steering input slew rates. Terminal stability costs on sideslip and lateral error help compensate for the finite horizon. Finally, track bounds are encoded as a slack constraint on minimum/maximum lateral error.

The efficacy of this approach is first demonstrated in a slalom drifting experiment on a racetrack, using a modified Toyota GR Supra. After being rapidly destabilised by a separate procedure, the NMPC controller takes over and smoothly performs dynamic, non-equilibrium drifting, while staying within the track bounds. It then seamlessly transitions to straight-ahead grip driving, ending the experiment. Repeating this experiment several times provides insight into the reliability and robustness of the controller, and provides ample data for validating the tire model. We also see instances of the controller flexibly transitioning in and out of the sliding tire regime to balance slack constraints with tracking objectives. Finally, a separate experiment demonstrates the controller's robustness to injections of significant longitudinal force and wheelspeed disturbances.

Indeed, it is hoped that this result could help enable autonomous vehicles of the future to reliably and confidently exceed stable handling limits if needed, potentially improving safety in edge case scenarios. Further work could continue to explore the potential benefits of unifying slip control – currently the domain of single-purpose modules (e.g. ABS/ESC) – with the higher-level predictive control layer. Concomitantly, crossing into the realm of these proven production features also creates a burden to investigate reliability and robustness.

## Acknowledgments

The authors would like to thank our colleagues at Toyota Research Institute, Toyota Motor Corporation, Toyota Motors North America, Toyota Racing Development, and Toyota Gazoo Racing for their kind support.

## Disclosure statement

No potential conflict of interest was reported by the author(s).

## References

- [1] Velenis E, Katzourakis D, Frazzoli E, et al. Steady-state drifting stabilization of RWD vehicles. *Control Eng Pract.* **2011 Nov**;19(11):1363–1376. doi: [10.1016/j.conengprac.2011.07.010](https://doi.org/10.1016/j.conengprac.2011.07.010)
- [2] Edelmann J, Plochl M. Handling characteristics and stability of the steady-state powerslide motion of an automobile. *Regul Chaotic Dyn.* **2009**;14(6):682–692. doi: [10.1134/S1560354709060069](https://doi.org/10.1134/S1560354709060069)
- [3] Voser C, Hindiyeh R, Gerdes JC. Analysis and control of high sideslip manoeuvres. *Veh Syst Dyn.* **2010**;48:317–336. doi: [10.1080/00423111003746140](https://doi.org/10.1080/00423111003746140)
- [4] Hindiyeh R, Gerdes JC. A controller framework for autonomous drifting: design, stability, and experimental validation. *J Dyn Syst Meas Control-trans Asme.* **2011**;136:051015. doi: [10.1115/1.4027471](https://doi.org/10.1115/1.4027471)
- [5] Ono E, Hattori Y, Muragishi Y, et al. Vehicle dynamics integrated control for four-wheel-distributed steering and four-wheel-distributed traction/braking systems. *Veh Syst Dyn.* **2006**;44(2):139–151. doi: [10.1080/00423110500385790](https://doi.org/10.1080/00423110500385790)
- [6] Tavernini D, Massaro M, Velenis E, et al. Minimum time cornering: the effect of road surface and car transmission layout. *Veh Syst Dyn.* **2013**;51(10):1533–1547. doi: [10.1080/00423114.2013.813557](https://doi.org/10.1080/00423114.2013.813557)
- [7] Oh S, Avedisov SS, Orosz G. On the handling of automated vehicles: modeling, bifurcation analysis, and experiments. *Eur J Mech A/Solids.* **2021**;90:104372. doi: [10.1016/j.euromechsol.2021.104372](https://doi.org/10.1016/j.euromechsol.2021.104372)
- [8] Fabio Della Rossa GM, Piccardi C. Bifurcation analysis of an automobile model negotiating a curve. *Veh Syst Dyn.* **2012**;50(10):1539–1562. doi: [10.1080/00423114.2012.679621](https://doi.org/10.1080/00423114.2012.679621)
- [9] Chaichaowarat R, Wannasuphoprasit W. Optimal control for steady state drifting of rwd vehicle. *IFAC Proc Volumes.* **2013**;46(21):824–830. doi: [10.3182/20130904-4-JP-2042.000557](https://doi.org/10.3182/20130904-4-JP-2042.000557)th IFAC Symposium on Advances in Automotive Control. Available from: <https://www.sciencedirect.com/science/article/pii/S1474667016384774>.
- [10] Zhou X, Hu C, Duo R, et al. Learning-based mpc controller for drift control of autonomous vehicles. In: 2022 IEEE 25th International Conference on Intelligent Transportation Systems (ITSC); 2022. p. 322–328.
- [11] Hindiyeh RY, Christian Gerdes J. A controller framework for autonomous drifting: design, stability, and experimental validation. *J Dyn Syst Meas Control.* **2014 Sep**;136(5):051015. doi: [10.1115/1.4027471](https://doi.org/10.1115/1.4027471)
- [12] Cutler M, How JP. Autonomous drifting using simulation-aided reinforcement learning. In: 2016 IEEE International Conference on Robotics and Automation (ICRA); IEEE; 2016. p. 5442–5448.
- [13] Werling M, Reinisch P, Gröll L. Robust power-slide control for a production vehicle. *Int J Veh Auton Syst.* **2015 Jan**;13(1):27–42. doi: [10.1504/IJVAS.2015.070727](https://doi.org/10.1504/IJVAS.2015.070727)
- [14] Goh JY, Goel T, Gerdes JC. Toward automated vehicle control beyond the stability limits: drifting along a general path. *J Dyn Syst Meas Control-trans Asme.* **2019**;142(2):021004. doi: [10.1115/1.4045320](https://doi.org/10.1115/1.4045320)
- [15] Goh J. Automated vehicle control beyond the stability limits [dissertation]. Stanford, CA: Stanford University; **2019**.
- [16] Laurence VA, Gerdes JC. Long-Horizon vehicle motion planning and control through serially cascaded model complexity. *IEEE Trans Control Syst Technol.* **2022 Jan**;30(1):166–179. doi: [10.1109/TCST.2021.3056315](https://doi.org/10.1109/TCST.2021.3056315)
- [17] Brown M, Gerdes JC. Coordinating tire forces to avoid obstacles using nonlinear model predictive control. *IEEE Trans Intell Veh.* **2020 Mar**;5(1):21–31. doi: [10.1109/TIV](https://doi.org/10.1109/TIV)
- [18] Dallas J, Thompson M, Goh J, et al. A hierarchical adaptive nonlinear model predictive control approach for maximizing tire force usage in autonomous vehicles. *Field Robot.* **2023 jan**;3(1):222–242. doi: [10.55417%2Ffr.2023006](https://doi.org/10.55417%2Ffr.2023006)
- [19] Brown M, Gerdes JC. Robust stabilization and collision avoidance through minimizing open-loop velocity uncertainty. In: 2020 IEEE Intelligent Vehicles Symposium (IV); 2020. p. 259–264.

- [20] Wurts J, Dallas J, Stein JL, et al. Adaptive nonlinear model predictive control for collision imminent steering with uncertain coefficient of friction. In: 2020 American Control Conference (ACC); 2020. p. 4856–4861.
- [21] Febbo H, Jayakumar P, Stein JL, et al. Real-time trajectory planning for automated vehicle safety and performance in dynamic environments. *J Auton Veh Syst.* **2021**;1(4):041001. doi: [10.1115/1.4053243](https://doi.org/10.1115/1.4053243)
- [22] Alsterda JP, Brown M, Gerdés JC. Contingency model predictive control for automated vehicles. In: 2019 American Control Conference (ACC); IEEE; 2019. p. 717–722.
- [23] Dallas J, Wurts J, Stein JL, et al. Contingent nonlinear model predictive control for collision imminent steering in uncertain environments. *IFAC-PapersOnLine.* **2020**;53(2):14330–14335. doi: [10.1016/j.ifacol.2020.12.13772](https://doi.org/10.1016/j.ifacol.2020.12.13772) 1st IFAC World Congress.
- [24] Svendenius J. Tire modeling and friction estimation [dissertation]. Lund, Sweden: Lund University; **2007**.
- [25] Fiala E. Seitenkrafen am rollenden luftreifen. *VdI.* **1954**;96:973–979.
- [26] Andersson JAE, Gillis J, Horn G, et al. CasADi – a software framework for nonlinear optimization and optimal control. *Math Program Comput.* **2019**;11(1):1–36. doi: [10.1007/s12532-018-0139-4](https://doi.org/10.1007/s12532-018-0139-4)
- [27] Wächter A, Biegler LT. On the implementation of an interior-point filter line-search algorithm for large-scale nonlinear programming. *Math Program.* **2006**;106(1):25–27.
- [28] Burt M. Greddy gr supra drift concept: supra to the max; 2019. Available from: <https://mag.toyota.co.uk/greddy-gr-supra-drift-concept/>.
- [29] Beal CE, Christian Gerdés J. Model predictive control for vehicle stabilization at the limits of handling; **2013**.
- [30] Bobier CG, Gerdés JC. Staying within the nullcline boundary for vehicle envelope control using a sliding surface. *Veh Syst Dyn.* **2013**;51(2):199–217. doi: [10.1080/00423114.2012.720377](https://doi.org/10.1080/00423114.2012.720377)